Title

TOUGH–RBSN simulator for hydraulic fracture propagation within fractured media: Model validations against laboratory experiments

Authors

Kim, Kunhwi
Rutqvist, Jonny
Nakagawa, Seiji
et al.

Publication Date

2017-11-01

DOI

10.1016/j.cageo.2017.05.011

Peer reviewed

TOUGH–RBSN simulator for hydraulic fracture propagation within fractured media: Model validations against laboratory experiments

Kunhwi Kim, Jonny Rutqvist, Seiji Nakagawa, Jens Birkholzer

Abstract

This paper presents coupled hydro-mechanical modeling of hydraulic fracturing processes in complex fractured media using a discrete fracture network (DFN) approach. The individual physical processes in the fracture propagation are represented by separate program modules: the TOUGH2 code for multiphase flow and mass transport based on the finite volume approach; and the rigid-body-spring network (RBSN) model for mechanical and fracture-damage behavior, which are coupled with each other. Fractures are modeled as discrete features, of which the hydrological properties are evaluated from the fracture deformation and aperture change. The verification of the TOUGH–RBSN code is performed against a 2D analytical model for single hydraulic fracture propagation. Subsequently, modeling capabilities for hydraulic fracturing are demonstrated through simulations of laboratory experiments conducted on rock-analogue (soda-lime glass) samples containing a designed network of pre-existing fractures. Sensitivity analyses are also conducted by changing the modeling parameters, such as viscosity of injected fluid, strength of pre-existing fractures, and confining stress conditions. The hydraulic fracturing characteristics attributed to the modeling parameters are investigated through comparisons of the simulation results.

Keywords: Coupled hydro-mechanical modeling, TOUGH2, Rigid-body-spring networks, Discrete fracture network approach, Hydraulic fracture propagation.

1. Introduction

Fracture initiation, propagation and reactivation due to pressurization of fluids are relevant to many geoengineering applications. For example, hydraulic fracturing and stimulation of fracture networks are utilized by the energy industry (e.g., shale gas extraction, enhanced geothermal systems, etc.) to increase permeability of geological formations (Freeman et al., 2011, Zimmermann and Reinicke, 2010). From the opposite perspective, related to nuclear waste disposal (Bossart et al., 2004, Levasseur et al., 2010) and underground CO_2sequestration (Chiaramonte et al., 2008, Pan et al., 2014), fracturing of the repository rock could be detrimental and increase the risk of contaminant leakage. Fluid-driven fracture propagation generally involves multiple physical phenomena associated with highly coupled hydro-mechanical (HM) processes, which should be taken into account for rational modeling.

Over the past decades, a number of mathematical models have been developed to help predict and interpret the fluid-driven fracture propagation (Khristianovic and Zheltov, 1955, Perkins and Kern, 1961, Geertsma and de

Klerk, 1969, Nordgren, 1972, Detournay, 2004). However, the model solutions are difficult to build because of the nonlinearity of the governing equation for the fluid flow in the fracture and the non-locality and time-dependence of the fracture responses. Especially in the presence of multiple fractures (e.g., propagating fractures and pre-existing natural fractures), the modeling of the fracture processes can be very challenging due to the complex interactions between propagating fractures and pre-existing fractures. In recent years, numerical algorithims, such as the pseduo-3D (P3D) model and the planar 3D model (PL3D), have been developed to simulate more realistic propagation of hydraulic fractures in multi-layered strata (Siebrits and Peirce, 2002, Adachi et al., 2007), but the simulations are limited to represent one crack lying in a single vertical plane.

Several recent studies have been made to model multiple fractures or fracture networks involved in coupled HM processes. Fu et al. (2013) proposed an explicit coupling simulation strategy for hydraulic fracturing in arbitrary discrete fracture networks. A finite-element based method is used for geomechanics simulations, in which a node-splitting scheme is featured for the adaptive remeshing to create new fracture faces. Pan et al. (2014) used a cellular automation coupled with a multiphase fluid flow simulator, TOUGH2 (Pruess et al., 2012), to represent multiple discontinuities and demonstrate multiple fracture interactions induced by CO_2 injection. Asahina et al. (2014) established a coupling framework between the TOUGH2 simulator and the rigid-body-spring network (RBSN) approach, and validated the TOUGH–RBSN code through simulations of swelling stress development and desiccation cracking in geomaterials. The simulation results indicated the potential abilities to model multiple fractures and discrete fracture interactions. However, building a robust and accurate numerical model that can properly address the coupled phenomena during hydraulic fracturing in complex fracture systems still remains a challenging task.

As a successive study using the TOUGH–RBSN simulator, this paper presents enhancements in the model construction and the TOUGH–RBSN coupling procedure to extend the modeling capabilities for tightly coupled HM responses of hydraulic fracturing within discrete fracture networks. A verification example is given for the 2D hydraulic fracture model, in which the resulting fracture aperture profiles are compared with the analytical solution of fracture geometries. Next, predictive simulations are conducted for fractured rock-analogue (soda-lime glass) samples in a laboratory experimental program. The model discretization scheme explained in this paper provides a close representation of the actual pre-existing fracture network. In addition, sensitivity analyses are conducted for qualitative interpretations by changing the injection parameters and reservoir configurations: viscosity of injected fluid; strength of pre-existing fractures; and confining stress conditions.

2. Methodology

2.1. Model discretization

The computational domain for both the TOUGH2 and RBSN calculations is tessellated using a Voronoi diagram (Okabe et al., 2000). The discretization process is carried out basically in three steps: 1) nodal point insertion; 2) Delaunay tessellation; and 3) Voronoi discretization. Within the domain, nodal points are positioned in regular or irregular formation. For random point generation, a minimum allowable distance l_{min} is used to define the desired nodal density of the unstructured grid. The Delaunay tessellation is conducted based on the nodal positions, where each Delaunay edge defines the nodal connection of the corresponding lattice element. Through the dual Voronoi tessellation, the spatial domain is collectively filled with discrete polyhedral cells that render the elemental volumes. More detailed procedure of the domain partitioning is presented elsewhere (Yip et al., 2005, Asahina and Bolander, 2011).

The Voronoi discretization is not only an effective method for partitioning a spatial domain, but is also an essential part of the RBSN model formulation. The Voronoi diagram serves to scale the element coefficients for the system equations. Also, the availability of sharing the same grid geometry for the TOUGH2 and RBSN models enables a tight coupling without any spatial interpolation of primary variables.

For the discrete fracture network (DFN) approach, fractures and such discontinuities are explicitly modeled within the Voronoi grid. Voronoi cells generally represent the matrix component in a geomaterial constitution, and pre-existing or newly generated fractures are placed on the Voronoi cell boundaries. The geometry of fracture networks (e.g., orientation, length, curvature) can be obtained by observational mapping data, computer-generated statistical reproductions, or mechanical simulation results. An example of the discretization procedure in 2D modeling involving a straight fracture is as follows:

1. Generate a Voronoi unstructured grid for the spatial domain.

2. Overlay the reference fracture trajectory onto the grid.

3. Test all connections of natural neighboring nodes to check if they cross the fracture. For example, compare connections *ij* and *jk* in Fig. 1.

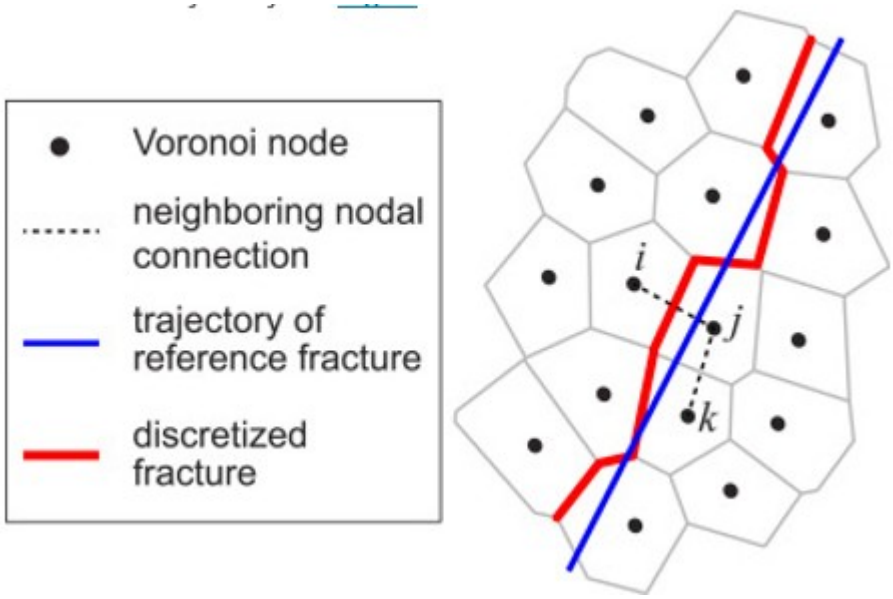

Fig. 1. Fracture mapping and discretization within an unstructured Voronoi grid (adopted from Asahina et al., 2014).

4. The collection of the Voronoi cell boundaries corresponding to the nodal connections that cross the reference fracture (such as *ij*) forms discretized fractures.

By repeating the above process for multiple fractures, a network of discrete fractures can be generated. This fracture discretization process is completely automated and can be easily extended to more complicated geometries in 3D modeling. However, the grid size should be carefully chosen to obtain a sufficiently precise representation of the reference fracture. A finer grid can accommodate the discretized fractures that conform more closely to the reference fracture. Still, a discrepancy of the total fracture length exists between the discretized and reference paths. The effective length of each fracture segment should be somehow adjusted to calculate accurate flow distance in the discrete fractures, which will be addressed in a future study.

2.2. Hydrological and mechanical coupling in TOUGH–RBSN

This section presents the linkage between the TOUGH2 simulator and the RBSN approach. Brief reviews and explanation of each modeling code are given, and then the coupling procedure is described. Although TOUGH–RBSN has the availability to simulate temperature changes and thermal effects on mechanical behavior, this paper focuses on only HM processes in fluid-driven fracture behavior.

2.2.1. TOUGH2 simulator

TOUGH2 is a general-purpose simulator for flow and mass transfer in porous and fractured media (Pruess et al., 2012). The modeling approach is based on the integral finite difference method, also called the finite volume method, thus possesses the advantage of being compatible with regular or

irregular grids in any spatial dimensions. It also allows for flexibility of modeling fractures embedded in a porous medium, by which the effects of fractures on hydro-mechanical responses can be investigated (Zhang et al., 2004, Rutqvist et al., 2013).

The TOUGH2 simulator has an applicability to diverse modeling problems by adopting various equation-of-state (EOS) modules. Note that the simulations presented in this paper adopt the most basic EOS1 module for the single-phase (liquid) state of a water component with isothermal conditions.

In the simulations using a grid structure of the ordinary Voronoi discretization, flow and mass transfer are enacted only through the connections of the neighboring Voronoi nodes (called cell-cell connections in Fig. 2a). However, if fracturing occurs within the matrix, substantial flow may arise through the fracture path. For the DFN approach, this paper proposes a modification of the grid structure, in which dynamic formation of flow channels along the fractures is facilitated by introducing additional interface nodes and the associated connections. As shown in Fig. 2b, an interface node is inserted where the cell-cell connection intersects the Voronoi cell boundary. The original cell-cell connection is divided into two cell-interface (and vice versa) connections by the interface node. In addition, the connections between the interface nodes are established to activate flow channels in discrete fractures.

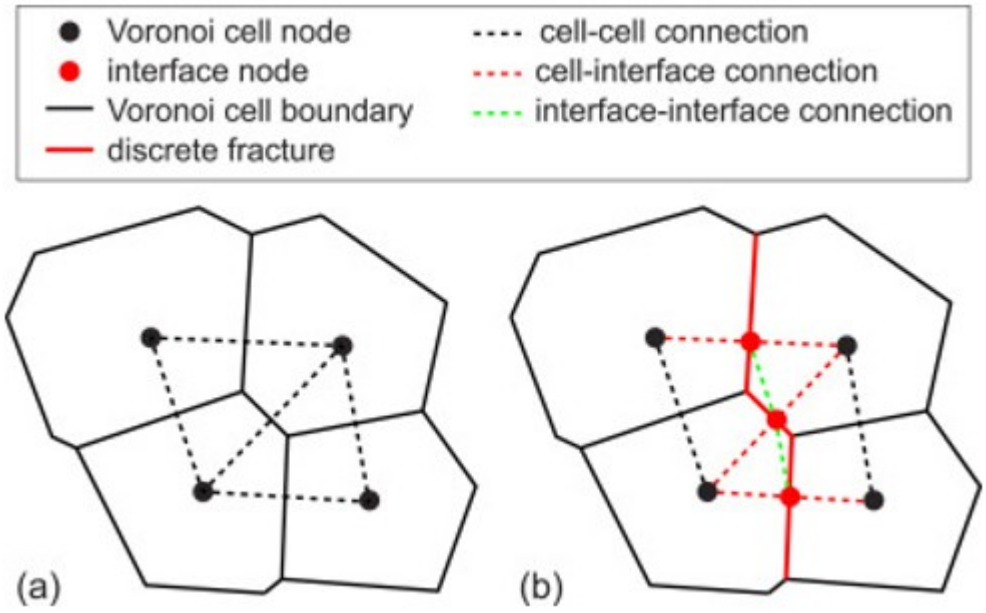

Fig. 2. Introduction of interface nodes and additional connections for flow through discrete fractures: a) original Voronoi cell nodes and connections; and b) insertion of interface nodes and connections.

Fluid flow through fractures is assumed to conform with Darcy's law, and hydrological properties (e.g., porosity and permeability) of a discrete fracture can be evaluated from the grid geometry and the fracture aperture width. The fracture aperture can be either assigned as a pre-existing fracture property or explicitly measured from the mechanical-damage computation of

the RBSN model. A parallel-plate model (Bear, 1972) is applied to define fracture permeability, which is related to a hydraulic aperture within the validity of cubic law for Darcy flow (Witherspoon et al., 1980).

2.2.2. Rigid-body-spring network

Elasticity and fracture-damage of geomaterials are modeled using the rigid-body-spring network (RBSN) approach. As a discrete modeling approach, the RBSN represents the mechanical system by a collection of simple lattice (two-node) elements. The lattice topology is defined by the Delaunay tessellation, and the dual Voronoi diagram is used to render the volume of a discretized domain (Fig. 3a).

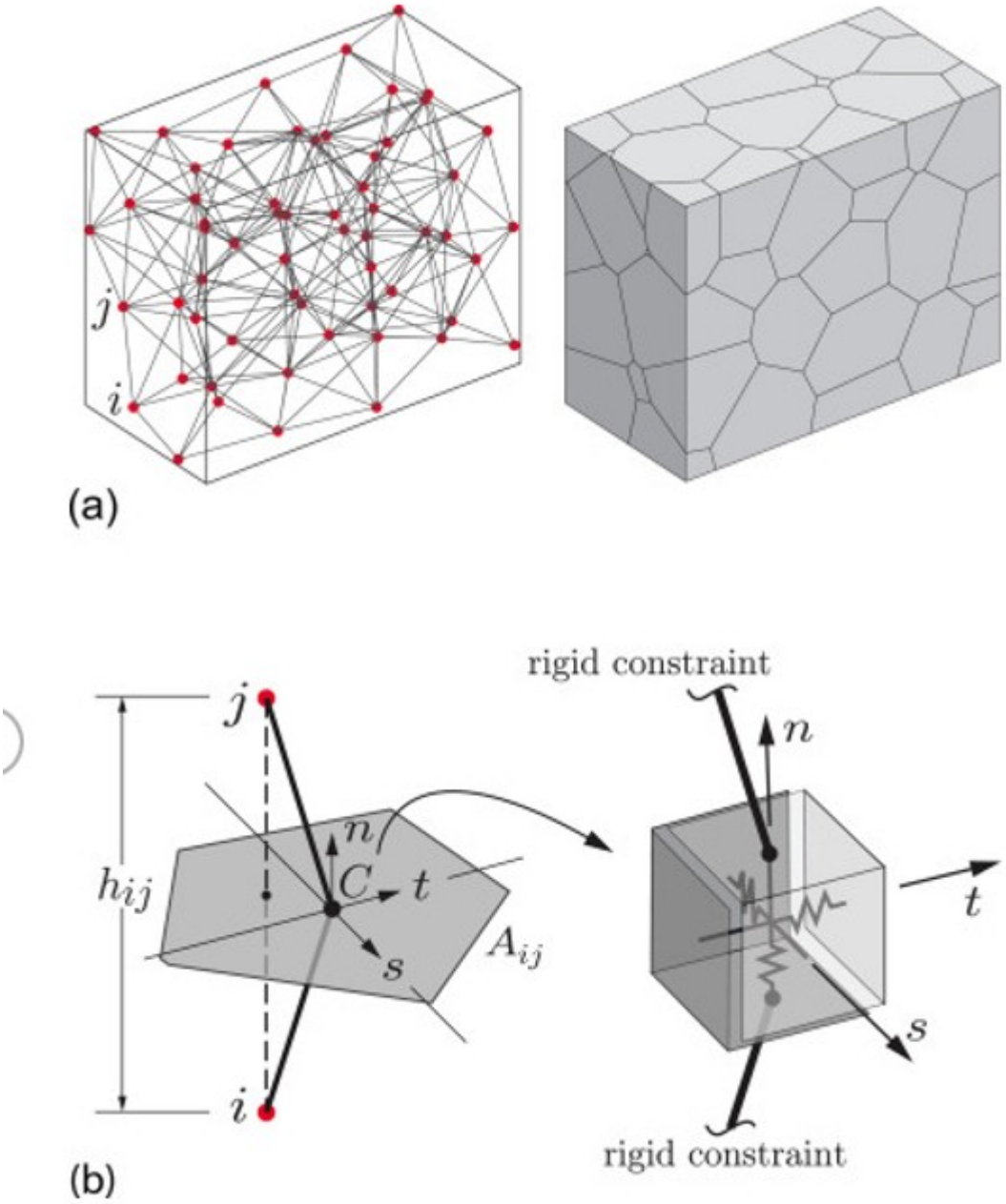

Fig. 3. Rigid-body-spring network modeling: a) Delaunay/Voronoi tessellations; b) lattice element *ij* with a zero-size spring set located at centroid *C* of area A_{ij}.

The elemental formulations are based on the rigid-body-spring concept (Kawai, 1978, Bolander and Saito, 1998). A lattice element consists of a zero-size spring set located at the centroid of the common Voronoi cell boundary and two rigid arm constraints that relate the spring set to the nodes (Fig. 3b). For 3D modeling, a spring set is formed from three axial springs and three rotational springs in local n−s−t coordinates. The n−axis is normal, and the s−t plane is parallel to the Voronoi cell boundary.

A diagonal matrix D=diag[kn,ks,kt,kϕn,kϕs,kϕt] consists of the six spring coefficients which are defined according to the geometrical properties of Voronoi diagram:

(1)ks=kt=α1kn=α1α2EAijhij,kϕn=EJphij,kϕs=EIsshij,kϕt=EItthij

where E is the elastic modulus, J_p, I_{ss}, and I_{tt} are the polar and two principal moment of area of the Voronoi cell boundary with respect to the centroid, respectively. The spring coefficients are scaled by the element length h_{ij} and the area of the Voronoi cell boundary A_{ij}. Effective Poisson ratio can be represented by adjusting α_1 and α_2. In this paper, by setting α1=α2=1, the models behave with elastic homogeneity under uniform straining, albeit with zero effective Poisson ratio (Asahina et al., 2011, Kim and Lim, 2011).

The fracturing process is represented by the damage/breakage of the springs. For a damaged spring set, the local spring coefficients are degraded as

(2)D′=(1−ω)D

where ω is a scalar damage index with a range from 0 (undamaged) to 1 (completely damaged).

A lattice element undergoes a fracture event when the stress state in the spring set violates the Mohr–Coulomb failure criterion (Fig. 4). The failure envelope is defined by three parameters: the internal friction angle β; cohesive strength c; and the tensile strength f_t(tension cut-off). To determine the criticality of the stress state, a stress ratio is calculated for each element I:

(3)RI=OPI¯/OPo¯

where PI(σn,σs,σt) represents a stress state applied in the three axial springs of element I, and P_o is the vectorial stress description of the point at which OPI¯ intersects the failure envelope. During nonlinear iterations, only one fracture event per iteration is allowed to arise at the element with the maximum stress criticality, i.e., RI=Rmax≥1. The fracture process in a local lattice element is realized by degrading the spring coefficient matrix D(Eq. (2)) and therefore releasing the stresses applied to the element. In this study, it is assumed that a single fracture event in a lattice element eliminates the spring coefficients at once (i.e., brittle fracture).

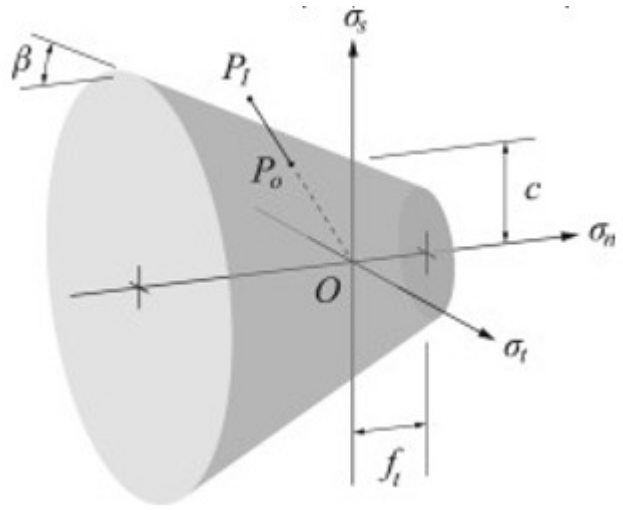

Fig. 4. Mohr–Coulomb fracture surface defined by intercept value c, friction angle β, and tension cut-off stress f_t.

2.2.3. TOUGH–RBSN coupling procedure

This section describes the linkage between the TOUGH2 simulator and the RBSN approach. The hydrological and mechanical codes are sequentially coupled to each other, where the general procedure is similar to that applied for the TOUGH–FLAC simulator (Rutqvist et al., 2002, Rutqvist, 2011). However, the TOUGH–RBSN coupling modules have been substantially modified to account for the fluid flow through discrete fractures.

In TOUGH-RBSN simulations, TOUGH2 is a main driver of analysis, which controls the time stepping during the coupling procedure, while the RBSN approach solves the mechanical response as a quasi-static process at each time step. The selection of small time steps is important to find stable solutions of the mechanical response, so the TOUGH2 input defines the upper limit for time step size with a small value to avoid any abrupt change of hydrological conditions over time steps.

Fig. 5 shows a schematic flow diagram of the coupling procedure between the TOUGH2 and RBSN codes. Coupling modules are implemented in each side of the modeling codes, by which material properties and mechanical boundary conditions are updated with the outputs of primary variables of physical quantities. As aforementioned, an advantage from sharing the same Voronoi grid geometry in the TOUGH–RBSN simulator is that the primary variables are highly correlated at the same nodal position and thus the data exchange between the two models is straightforward during the coupling procedure.

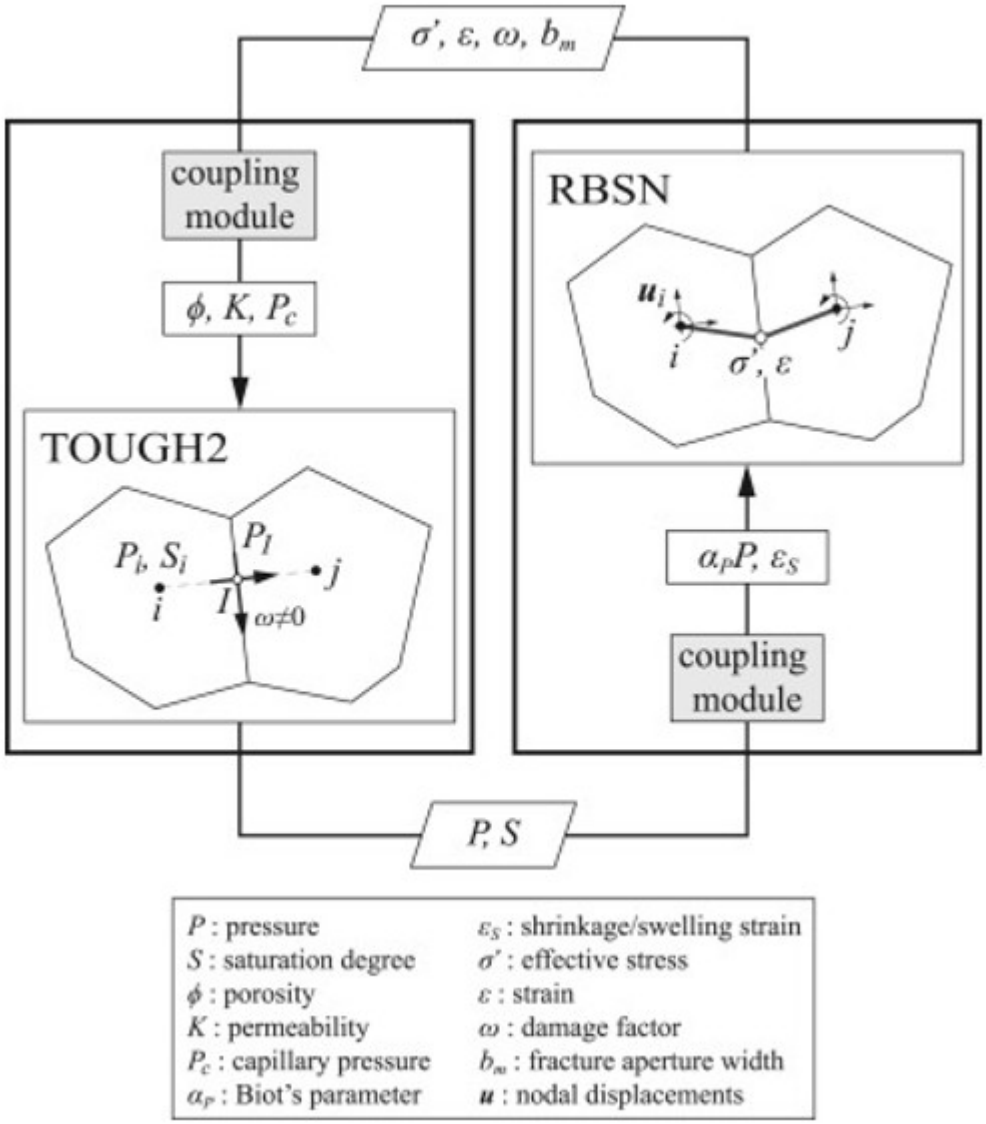

Fig. 5. Flow diagram of the TOUGH–RBSN coupling procedure. Note that the additional interface nodes and connections are activated in TOUGH2 when the corresponding RBSN elements are fractured (i.e., ω≠0).

First, the TOUGH2 to RBSN link supplies pressure and degree of saturation to update the mechanical quantities. From the pore pressure *P*, the effective (grain-to-grain) stress σ′n, applied to the normal spring of a lattice element, is calculated using Biot's theory (Biot and Willis, 1957):

(4)σ′n=σn+αpP

where σ′n is the total normal stress obtained from overall loading, including external loads; α_p is Biot's effective stress parameter. Note that tensile stress is taken to be positive for the sign convention in this paper. The effective stress in a lattice element *ij* can be calculated by averaging the

pressure at nodes *i* and *j*, for which Eq. (4) is transformed into an incremental form:

(5)Δσ′n=Δσn+αp(ΔPi+ΔPj)/2

where ΔPi and ΔPj are the pressure increments at nodes *i* and *j*, respectively. If the element *ij* corresponds to an interface node *I* for the activated fluid flow through the fracture, the effective stress increment can be described as

(6)Δσ′n=Δσn+αpΔPI

where ΔPI is the pressure increment at node *I* in the TOUGH2 model. Also, the shrinkage/swelling effect due to the local changes of liquid saturations can be taken into account:

(7)Δεs=αs(ΔSi+ΔSj)/2

where ε_s is a shrinkage/swelling strain; and α_s is the hydraulic shrinkage coefficient. If a poroelastic geomaterial is subjected to confinement conditions, the effective stress can be affected by the swelling/shrinking strain as

(8)Δσ′n=ΔεsE

Next, the RBSN to TOUGH2 link supplies the effective stress and the strain calculated in the lattice element to update the hydrological properties of the corresponding TOUGH2 grid blocks *i* and *j*. Porosity, permeability, and capillary pressure are generally related with the effective stress and strain values (Rutqvist and Tsang, 2002).

If fracturing occurs at element *ij* (i.e., ω≠ 0), the associated fracture node *I* and additional connections are activated in the TOUGH2 model. The permeability of an individual fracture depends on the hydraulic aperture b_h (Witherspoon et al., 1980). According to a parallel-plate model, the fracture permeability is defined as bh2/12. The hydraulic aperture is coupled to the mechanical aperture b_m (Rutqvist et al., 1998, Rutqvist et al., 2000):

(9)bh=bhr+fbm

where b_{hr} is the residual hydraulic aperture and f≤1.0 is a dimensionless factor that accounts for the slowdown of flow in a natural rough fracture in comparison to the ideal case of parallel smooth fracture surfaces. However, herein *f* is set equal to unity for simplicity.

2.3. Verification example: single straight fracture propagation

This section presents the validity of the developed coupling procedure in the TOUGH–RBSN simulator for hydraulic fracture simulations. A 2D rectangular domain with dimensions of 100×120 m is prepared as shown in Fig. 6. An unstructured Voronoi grid is generated with graded nodal density for computational efficiency, and a fracturing path is prescribed in the middle of the domain to provoke a single straight fracture propagation. The fluid

injection is applied at the left end of the prescribed fracture path. Mechanical and hydrological symmetric boundary conditions are applied at the left side of the domain, so that the model implies another identical fracture wing on the other side of the domain, which grows towards the left. Top and bottom edges are constrained with slipping (roller) boundary conditions. A soda-lime glass is adopted as the domain material, which will be also used for further hydraulic fracturing simulations presented hereafter. A detailed description of the mechanical and hydrological properties of the glass material is provided in Section 3.

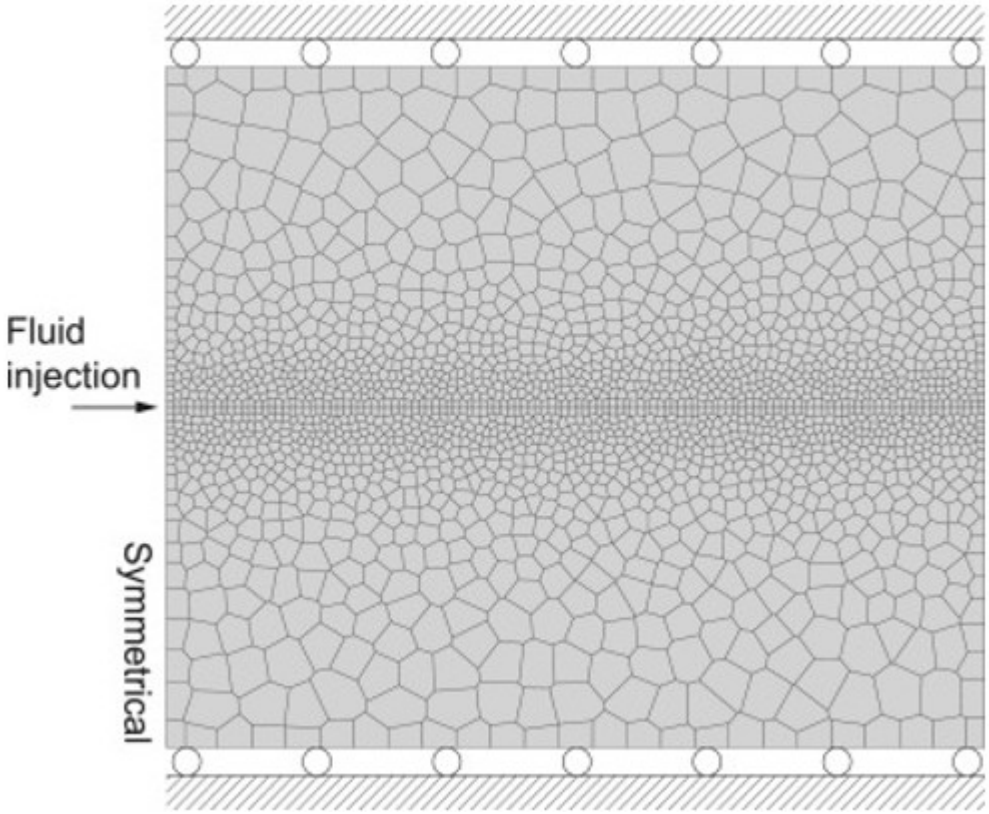

Fig. 6. Model set up for hydraulic fracturing simulation of a single fracture propagation.

Fig. 7a shows a snapshot of the fracture deformation at 20 s of fluid injection. During the simulation, a fracture aperture width can be explicitly measured as the generalized displacement of the lattice element along the fracture path. In Fig. 7b, the fracture aperture widths are plotted at 10, 15, and 20 s of fluid injection. The aperture width and length of the hydraulic fracture increase with the duration of fluid injection. Classical 2D fracture models, such as the Khristianovic–Geertsma–de Klerk (KGD) model (Khristianovic and Zheltov, 1955, Geertsma and de Klerk, 1969) and the Perkins–Kern–Nordgren (PKN) model (Perkins and Kern, 1961, Nordgren, 1972), indicate the cross section of a sufficiently long fracture to be elliptical based on the linear elastic fracture mechanics theory and the uniform fluid pressure condition along the fracture length. As the hydraulic fracture

propagates, the fracture aperture profiles retain elliptical shapes, which are in good agreement with the profiles analytically drawn for the crack opening displacement at the injection point and the crack length taken as the radii of an ellipse.

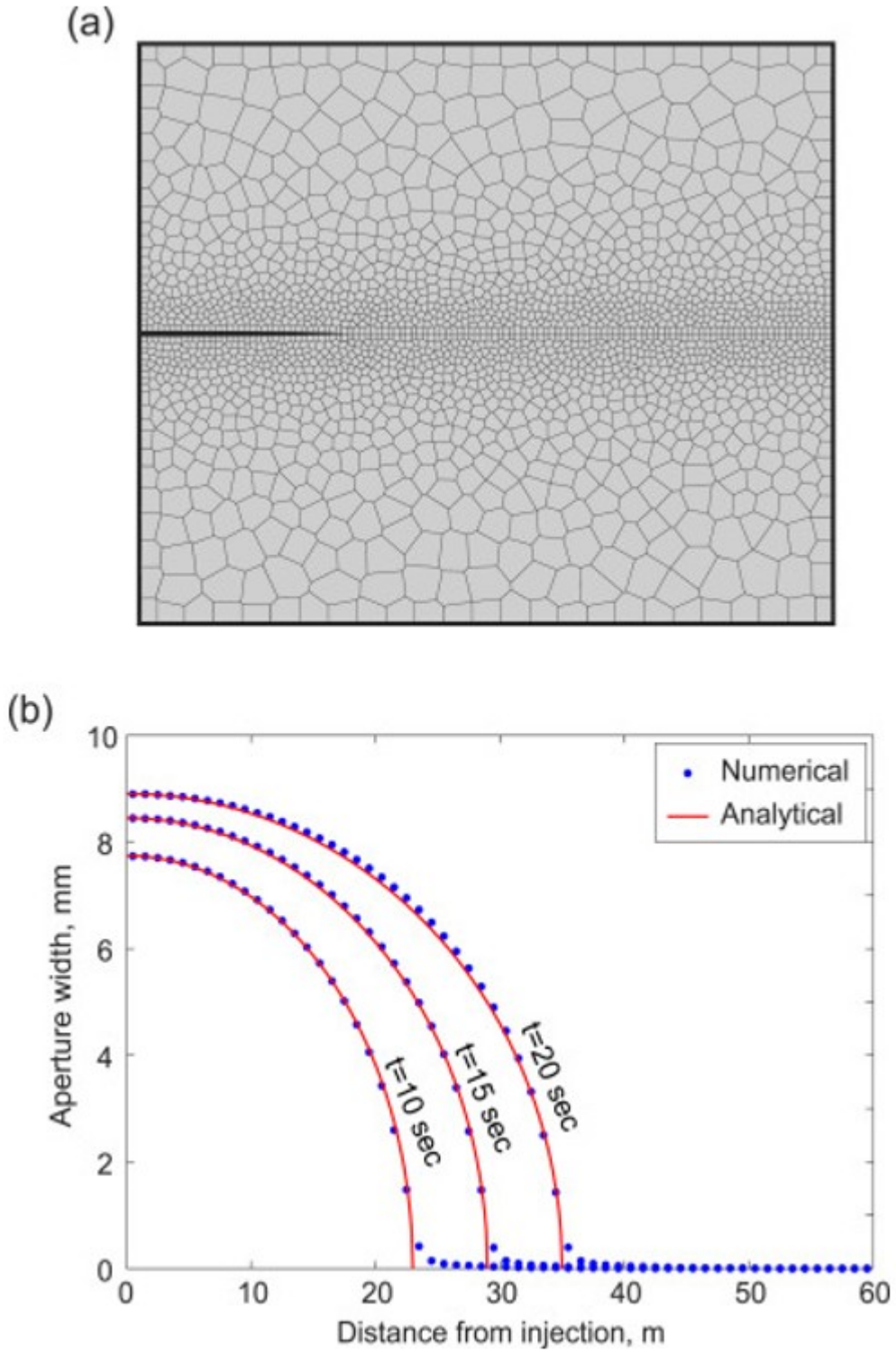

Fig. 7. a) Fracture deformation (×100 exaggerated); and b) comparison between the numerical model and the analytical approximation in terms of fracture aperture profiles.

3. Hydraulic fracturing in rock-analogue samples

3.1. Model description

The coupled HM modeling has been conducted in parallel with laboratory hydraulic fracturing propagation experiments. The experimental program used soda-lime glass blocks in which artificially created fractures provided some analogy to naturally fractured rock. A complex pre-existing fracture network was designed and embedded within the specimens (Fig. 8a), using the laser-engraving technique. With this technique, a fracture is represented by a planar cloud of thermally induced, isolated micro-cracks. During the laboratory experiment, a 3.2 mm diameter hole was drilled at the center of a glass block, and a stainless steel tube was inserted and cemented in place. This block was then confined using a true-triaxial (polyaxial) press, by applying anisotropic principal stresses of $\sigma x:\sigma y:\sigma z=4.83:7.24:9.67$MPa, where the *z*–direction is perpendicular to the plane of fracture network. Fluid was injected into the analogue borehole at a controlled injection rate using a motor and screw-driven piston pump, and hydraulic fractures were induced in the sample. Note that comparison between the laboratory experiment and the numerical modeling below is somewhat qualitative because the fracture network in a laboratory sample is three-dimensional (a 2D fracture network stretched in the depth direction) while the numerical model assumes a thin 3D slab containing a pervasive 2D network.

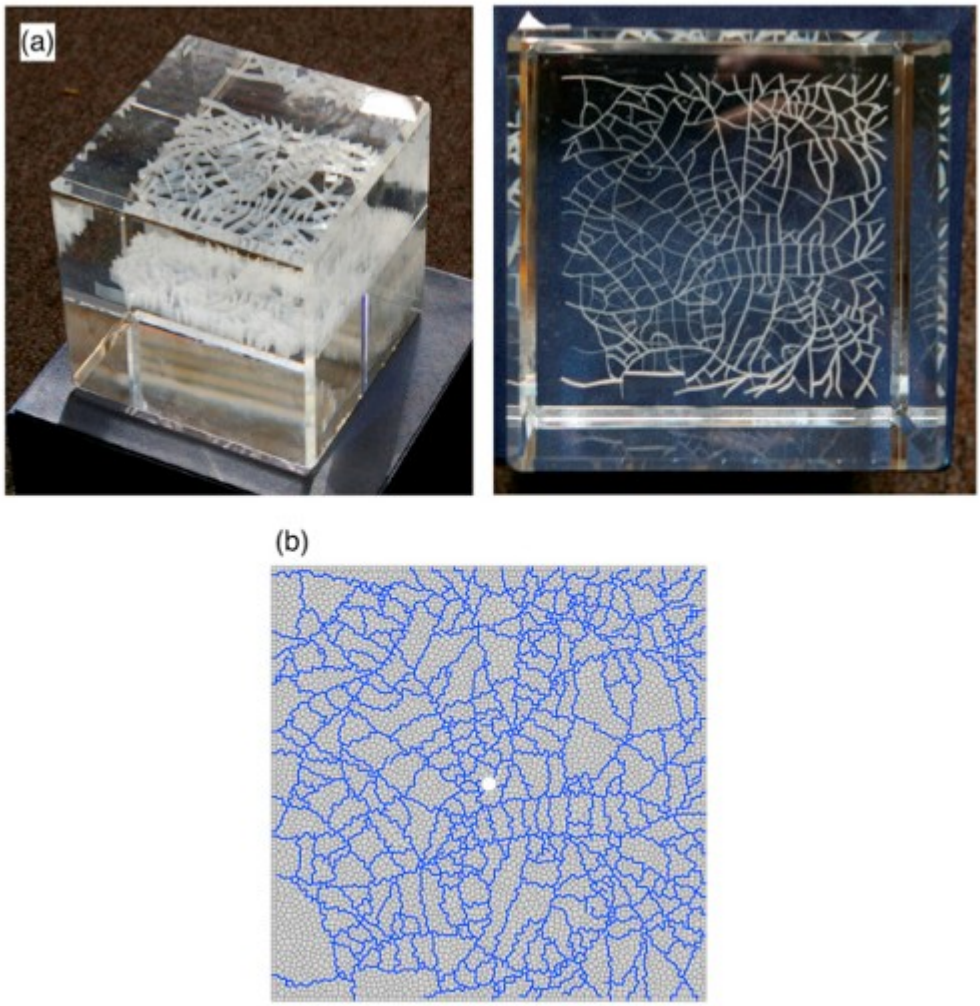

Fig. 8. Physical and numerical representations of complex pre-existing fractures: a) 3D laser-engraved fractures in a glass block; and b) mapping of the fracture network onto a unstructured Voronoi grid.

For model preparation, a 90 mm square domain containing a 3.2 mm diameter borehole at the center is discretized, and the pre-existing fractures are replicated by mapping the designed pattern onto the unstructured grid, as described in Section 2.1. Fig. 8b depicts details of the fracture network modeled in the Voronoi grid. Mechanical properties of the glass material are set as follows: Young's modulus E=73.8 GPa; tensile strength ft=11.3MPa; cohesive strength c=8.5MPa and internal friction angle β=25° for the Mohr–Coulomb failure criterion. Because the experiments did not characterize the strength parameters, these numbers are adopted from the literature for typical soda-lime glass (Wereszczak et al., 2011) or determined through a calibration process presented in Section 3.2. It is simply assumed that the glass material is impermeable, non-porous, and incompressible. Also, all the interface nodes, which represent fractures in the TOUGH2 simulation, are initially set to be impermeable. For an activated pre-existing fracture or a newly generated fracture, the corresponding interface node undergoes a

permeability increase, which is calculated based on the hydraulic aperture as suggested by Eq. (9).

The specimen is subjected to anisotropic confining stresses, σx:σy=4.83:7.24MPa, and water is injected into the borehole at a constant rate. Because the glass is prone to brittle fracturing, the injection rate should be carefully selected to make the fracture initiation and propagation as stable as possible (and therefore, observable). The injection rate is $3.8\times10-5$ cm^3/s per unit centimeter thickness, which is roughly estimated from the injection volume history in the actual laboratory experiments.

3.2. Hydraulic fracture propagation in intact glass blocks

Hydraulic fracturing simulations are performed for intact glass blocks to determine other unknown parameters through a calibration process. By setting the mechanical properties of the pre-existing fracture elements same as those of the glass domain, the fractured glass block can convert into the intact glass block while preserving the grid geometry and modeling configurations described in Section 3.1.

With the given injection rate, the compressibility of the borehole is adjusted to $5.0\times10-9$ Pa^{-1}. The injection pressure evolution is plotted in Fig. 9, where the simulated pressurization rate, denoted by the slope of the ascending branch, is fitted to the experimental result for an intact borehole. The preset/calibrated hydrological properties are listed in Table 1.

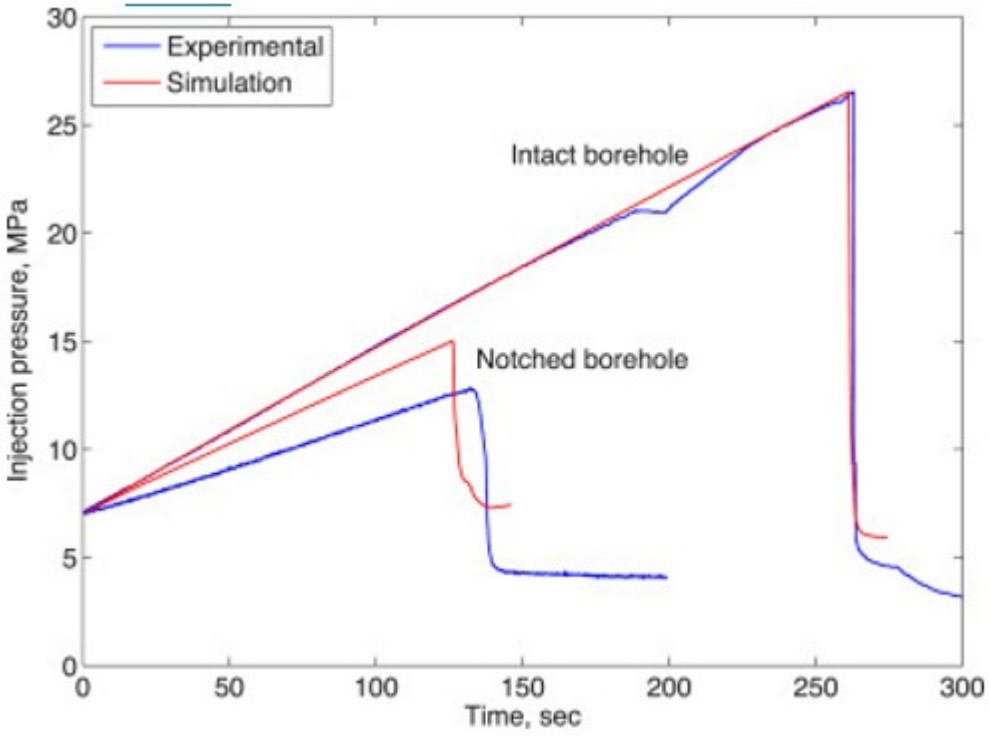

Fig. 9. Injection pressure evolutions for hydraulic fracturing of intact glass blocks.

Table 1. Hydrological properties of glass, fracture, and borehole domains.

Domain		Permeability (m^2)	Porosity (-)	Pore compressibility (Pa^{-1})
Glass		0	0	0
Fracture	Pre-existing	0	0	0
	activated	bh2/12†	0.8	3.0×10−8
Borehole		1.0×10−9	0.8	5.0×10−9

† The permeability of an activated fracture depends on the hydraulic aperture width, which is evaluated by Eq. Eq. (9) with an assumption for the residual hydraulic aperture bhr=0.25μm.

Fig. 10 shows snapshots of the fracture traces and the pressure distributions over time. The breakdown point is captured at time t_0, from which the time lapse during fracture propagation is counted as τ=t−t0. Two fracture branches stretch out from the borehole and propagate mainly in the direction parallel to the maximum confining stress. As the fractures advance, the injected fluid transfers into the empty space created by the fractures. The fracture paths reflect higher pressure contrasting to the surrounding glass matrix, and accordingly the injection pressure decreases at the borehole. Further fracture growth occurs at one branch reaching the upper boundary in 2 s. Such rapid and instantaneous fracture propagation makes it difficult to observe details of interactions between pre-existing fractures and hydraulic fractures in the experiments.

To stabilize the fracture growth, pre-cracks or notches are introduced around the borehole. Strain singularity and stress concentration arise at the crack tips (Rice, 1968), which is expected to advance the fracture initiation with a lower triggering pressure and thus provide a gradual fracture propagation. In the experimental program, a small flaw is generated by mechanically compressing a rubber plug at the bottom of the borehole. This method generates stable pre-cracks by pressurizing the borehole wall (Fig. 11a). The orientation of the flaw can be controlled to some degree by applying confining stresses to the specimen during the pressurization. In the numerical models, notches or other types of discontinuities (e.g., defects, fault planes, etc.) are represented by breaking/damaging the elements. From the resulting fracturing paths for the intact borehole presented in Fig. 10, the fractured interface segments are manually picked to introduce the notches around the borehole (Fig. 11b), in which the mechanical resistance is completely removed in tension and small permeability and porosity are introduced.

The injection pressure evolution of the notched borehole is plotted and compared with that of the intact borehole in Fig. 9. The injection pressure increases at a lower rate in the pre-peak region, which is attributed to infiltration of the injected fluid into the notches. The breakdown occurs at a lowered peak pressure as expected and the pressure is gradually released in the post-peak region, which implies a slower fracture propagation with the notched borehole. Both the simulations and the laboratory tests demonstrate that the fracture growth is slower in the case of the notched borehole. However, a disagreement exists on the peak pressure and the pressurization rate between the simulation and experimental results. These quantitative discrepancies may be because it is difficult to precisely measure the length of the pre-cracks and therefore they may not be correctly represented in the model.

A comparison between Fig. 10, Fig. 11, Fig. 12 explicitly explains the effects of the notched borehole on the rate of fracture growth. The fracturing speed is significantly reduced with the notched borehole, in which about 5–10 times longer period of time is taken for the same extent of fracture propagation. Moreover, a low level of the triggering and driving pressure evolves during the fracturing process with the notched borehole, and therefore the fracture is arrested after reaching a certain length (at τ=8.00 s) and then the fracture front proceeds very slowly while the fluid injection is continued at a constant rate.

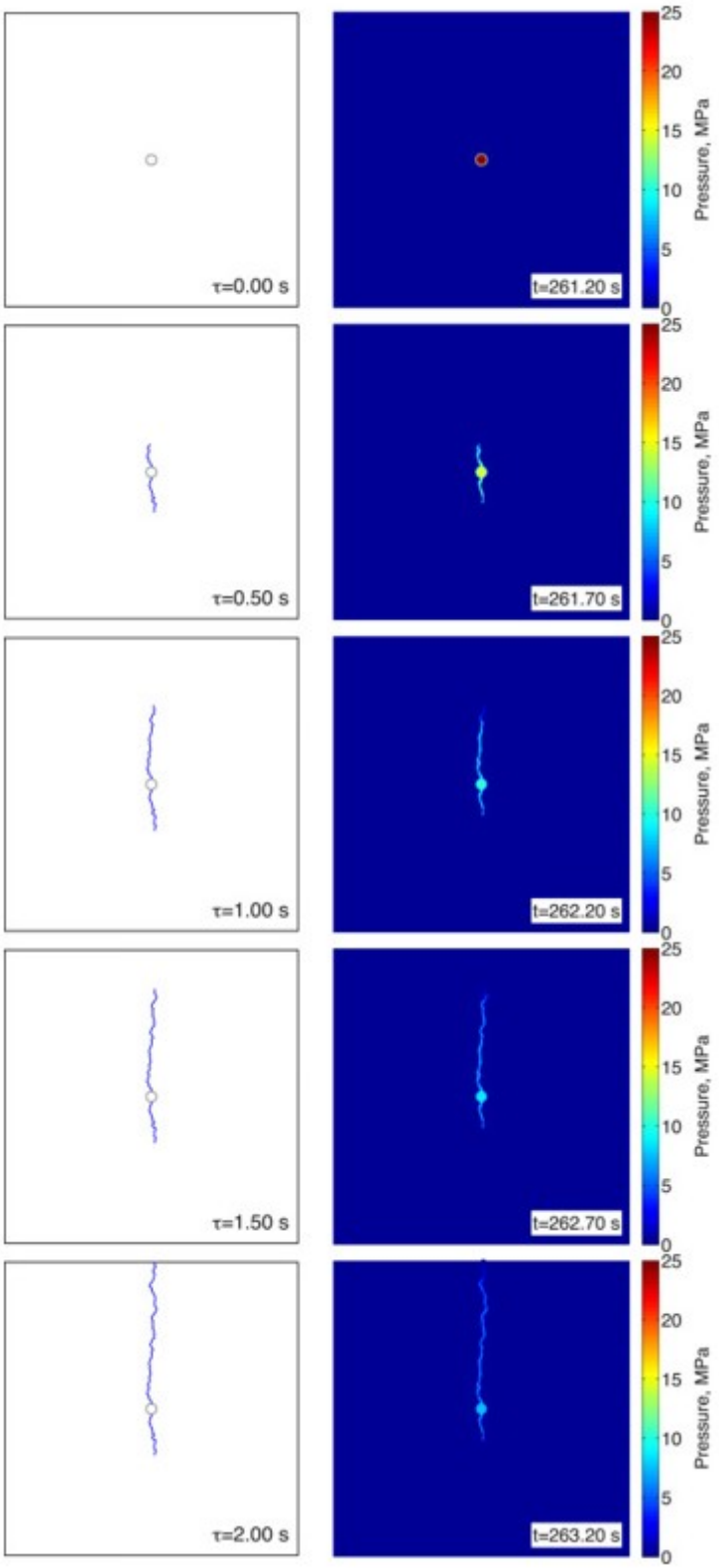

Fig. 10.

Snapshots of the fracture traces and the pressure distributions during fracture propagation from the intact borehole.

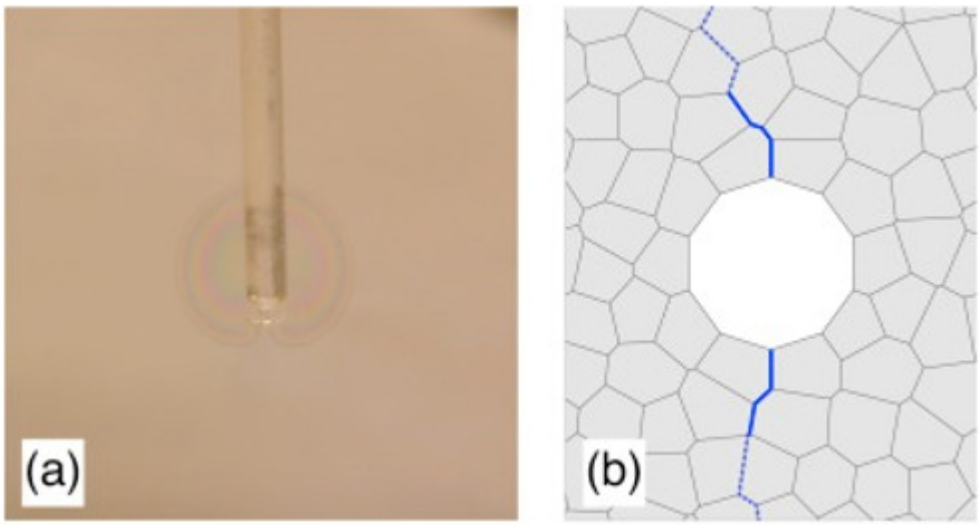

Fig. 11. Introduction of initial notches around the borehole: a) pre-cracking of a test sample; and b) modeling of the notches by selecting fractured segments (illustrated by blue solid lines).

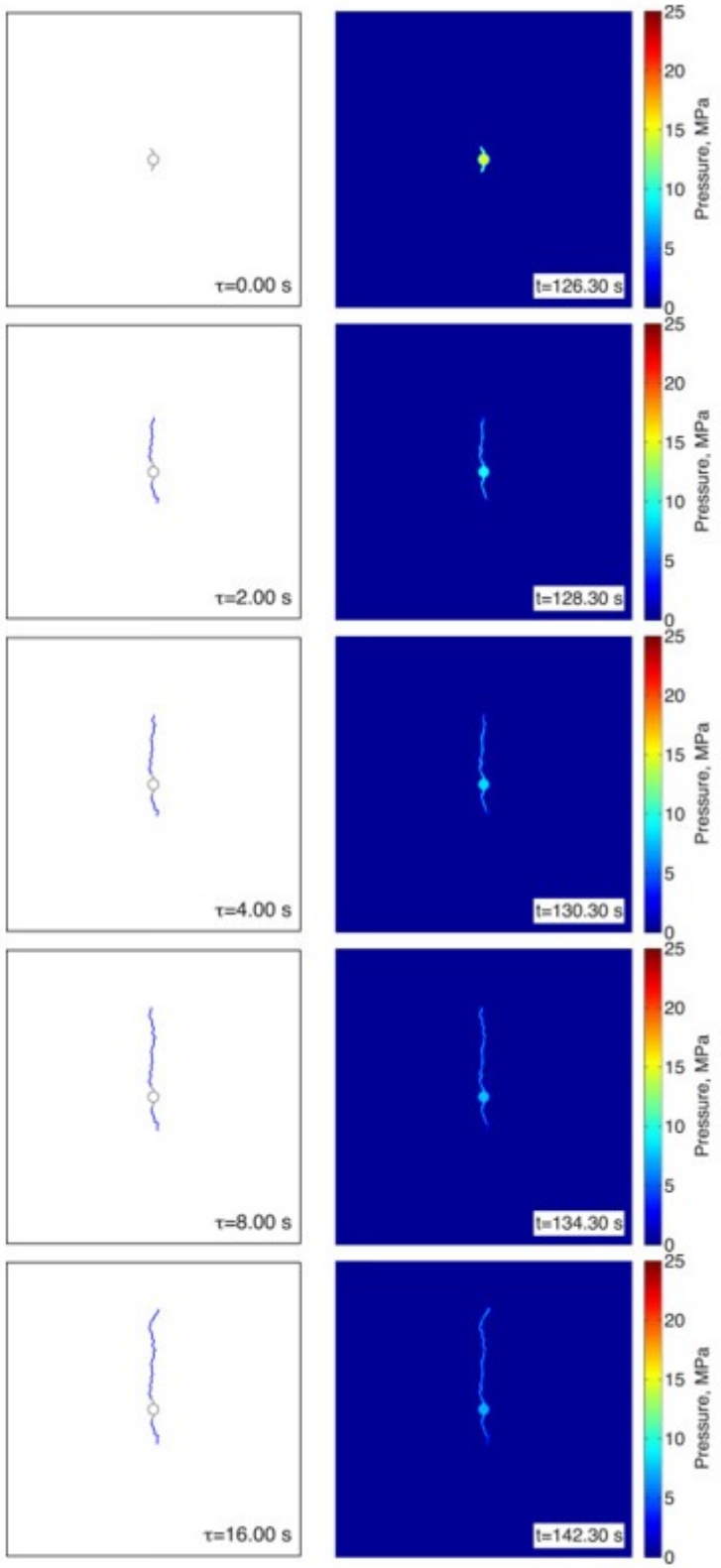

Fig. 12. Snapshots of the fracture traces and the pressure distributions during fracture propagation from the notched borehole.

3.3. Hydraulic fracture propagation in the presence of pre-existing fractures

Within the same model description presented in Section 3.1, a fractured glass block is modeled by assigning weaker and more compliant mechanical properties to the lattice elements which correspond to the pre-existing fractures. The mechanical properties of the pre-existing fractures can be varied based on the expected weakening in accordance with the density of the etched micro-cracks forming the fracture network (Fig. 8a). For the simulation presented in this section, Young's modulus, the tensile strength, and the cohesive strength are initially reduced by half from those of the intact glass material, whereas the internal friction angle is retained. The notches around the borehole are modeled in the same way described in Section 3.2, but from the result of a preliminary simulation the fractured segments are taken at different locations mainly corresponding to the pre-existing fractures. Hydrological properties of the material domains conform with the values in Table 1. Note that the pre-existing fractures are assumed to be initially impermeable, thus they do not affect the hydrological behavior unless activated.

The resulting fracture trace shows that the direction of hydraulic fracturing is influenced by a combination of the anisotropic stress condition and the degraded mechanical properties of the pre-existing fracture network (Fig. 13a). Two main fracture branches propagate from the borehole in the direction sub-parallel to the maximum confining stress with a slight perturbation due to the local heterogeneity of pre-existing fractures. The fracture branches mostly follow the activated pre-existing fractures (depicted by blue lines), and at some locations cut-throughs are made by newly generated fractures (depicted by red lines). The overall shape of the simulated fracture trace agrees well with the visualized hydraulic fracturing paths in the laboratory test (Fig. 13b). However, the fracture paths in the upper branch show a noticeable disagreement between the simulation and experimental results, which may be attributed to mesh bias in the discrete modeling of fractures (Bolander and Saito, 1998) as well as heterogeneous properties of pre-existing fractures.

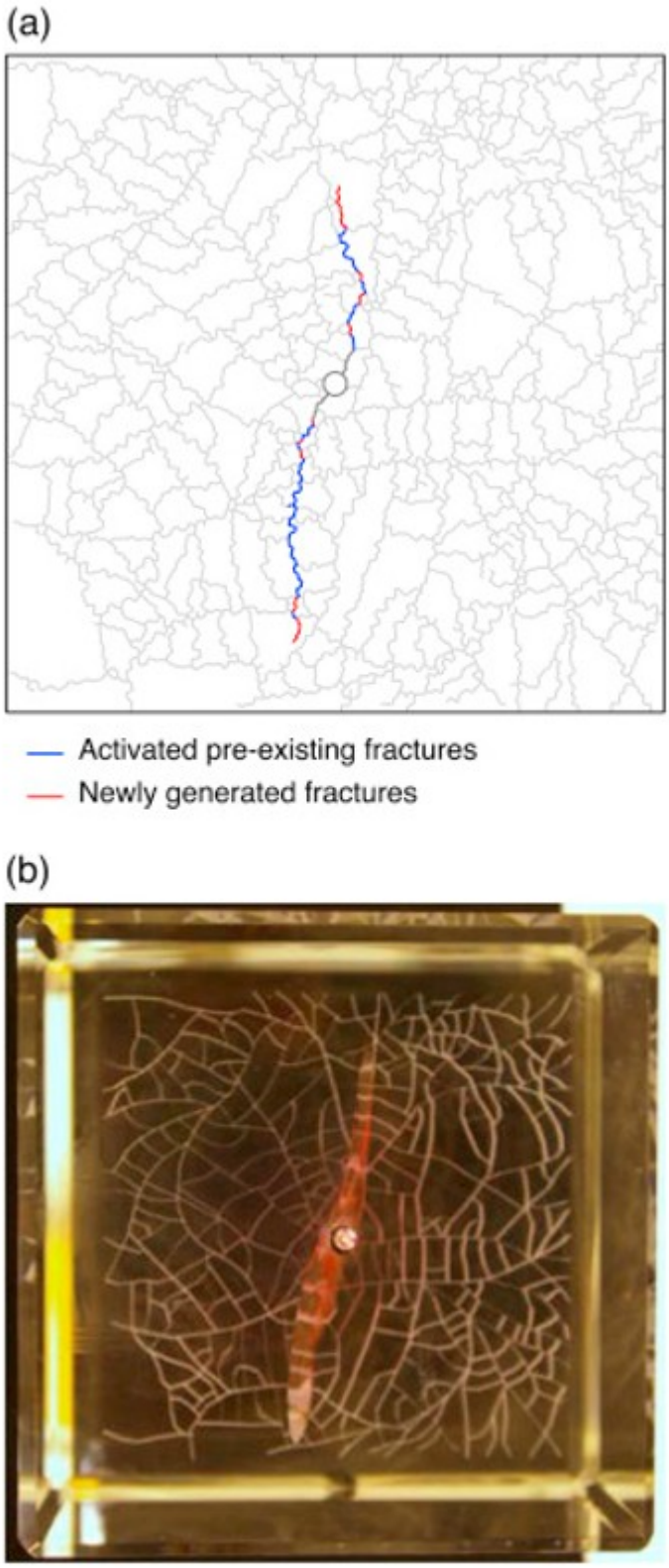

Fig. 13. A comparison between a) the simulated fracture trace within the pre-existing fractures and b) the visualization of hydraulic fractures in the laboratory test.

This simulation is taken as a control model for the following sensitivity analyses. In the next section, interpretative simulations are performed by changing the model factors: viscosity of injected fluid; strength of pre-existing fractures; and confining stress conditions, which can affect the characteristics in the hydraulic fracturing responses. Further discussions on the simulation results will be made through qualitative comparisons with other modeling cases.

4. Sensitivity analyses of hydraulic fracture propagation

4.1. Viscosity of injected fluid

The effect of the viscosity of injected fluid on the hydraulic fracture propagation is investigated with two different fluid viscosities: 1 and 1100 cP, which correspond to water (control) and glycerol, respectively. The TOUGH2 simulator is capable of representing different fluid mixtures by adopting the user-specified EOS modules. Alternatively, in this study, a viscosity parameter has been coded in the main TOUGH2 module while the same EOS module (e.g., EOS1 for a water component) is applied, which can provide more freedom to program users with a provisional modification.

Fig. 14 compares the injection pressure evolutions, which indicate that the high viscosity of injected fluid (glycerol) leads to a slower fracture propagation with a more gradual pressure decrease after the breakdown. For the case of glycerol injection, a steeper initial pressurization rate and therefore a higher peak pressure are shown in the pre-peak region, and distinctively the breakdown is shifted to the post-peak region. The pressurization of injected glycerol starts to decelerate around 150 s of injection time, at which the hydraulic fracture is not triggered yet. Those time-dependent features are also observed and discussed in the laboratory tests, which may be attributed to a significant delay of the initial infiltration of glycerol into the notches, trapping the viscous fluid in the borehole until the pressurized fluid mechanically opens the notches to significantly raise fracture transmissivity. This attribution is evidenced by Fig. 15, which arranges the snapshots of notch deformations and pressure distributions in the vicinity of the borehole. Fig. 15a displays an immediate infiltration of the water, in which the fluid pressure is uniformly distributed at the borehole and through the notches with infinitesimal deformations. On the contrary, as shown in Fig. 15b, the glycerol exhibits a stagnant flow forming a gradient of fluid pressure along the notch length, and the fluid front does not proceed until the notch opening is sufficiently large to bring about the infiltration.

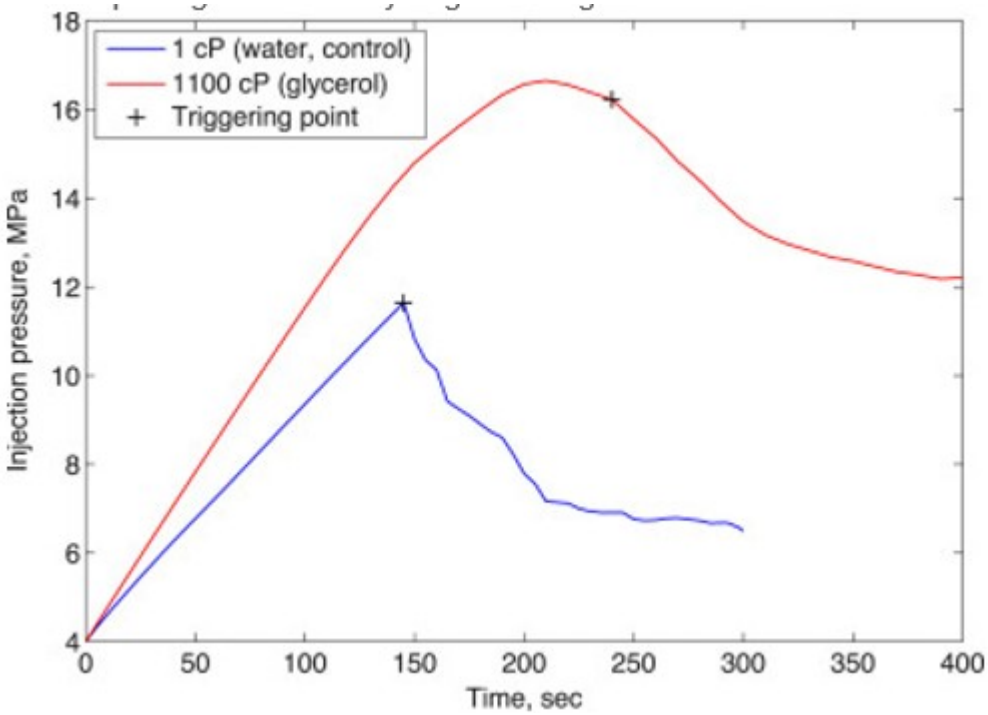

Fig. 14. Injection pressure evolutions for the cases of different fluid viscosities.

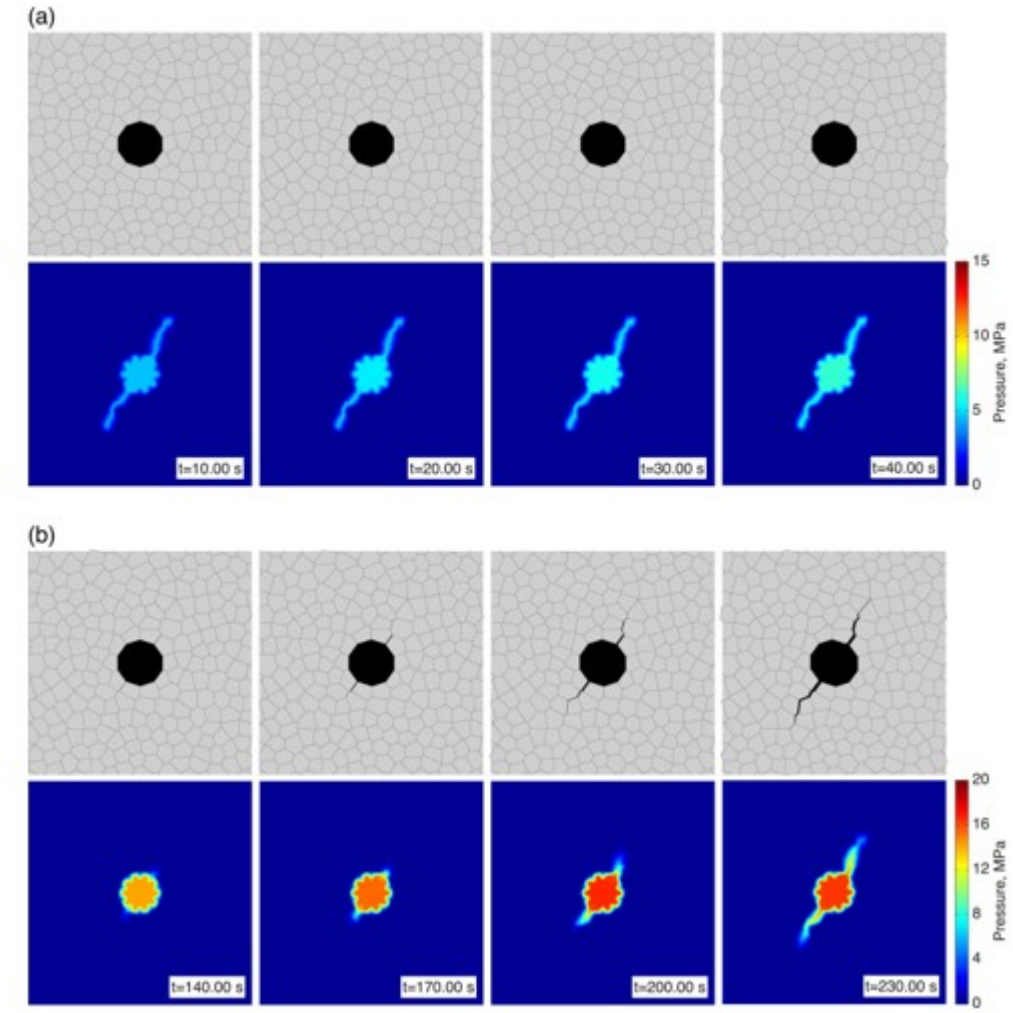

Fig. 15. Evidence of fluid infiltration into initial notches by means of notch deformations (×100 exaggerated) and pressure distributions: a) low-viscosity water (control); and b) high-viscosity glycerol.

Fig. 16 presents fracture traces and pressure distributions at the final stage of the simulations. There is no apparent difference in the resulting fracture traces, however a comparison of the pressure distributions interprets that entirely different mechanisms are involved in the fracture propagations. For the case of water injection (Fig. 16a), the elevated fluid pressure coincides with the entire length of the fracture trace, which reflects a uniform pressure distribution. In a local sense, the fluid pressure at the fracture tip is more likely to stimulate the fracture propagation. For the case of glycerol injection (Fig. 16b), by comparison, a diminishing fluid pressure is shown with increasing distance from the borehole and the realized pressure elevation is much shorter than the fracture trace, which indicates the existence of a gap between the fracture tip and the fluid front. Consequently, the results explain that the non-local effect of remote pressure is a dominant mechanism of hydraulic fracture propagation when the fracturing fluid is highly viscous.

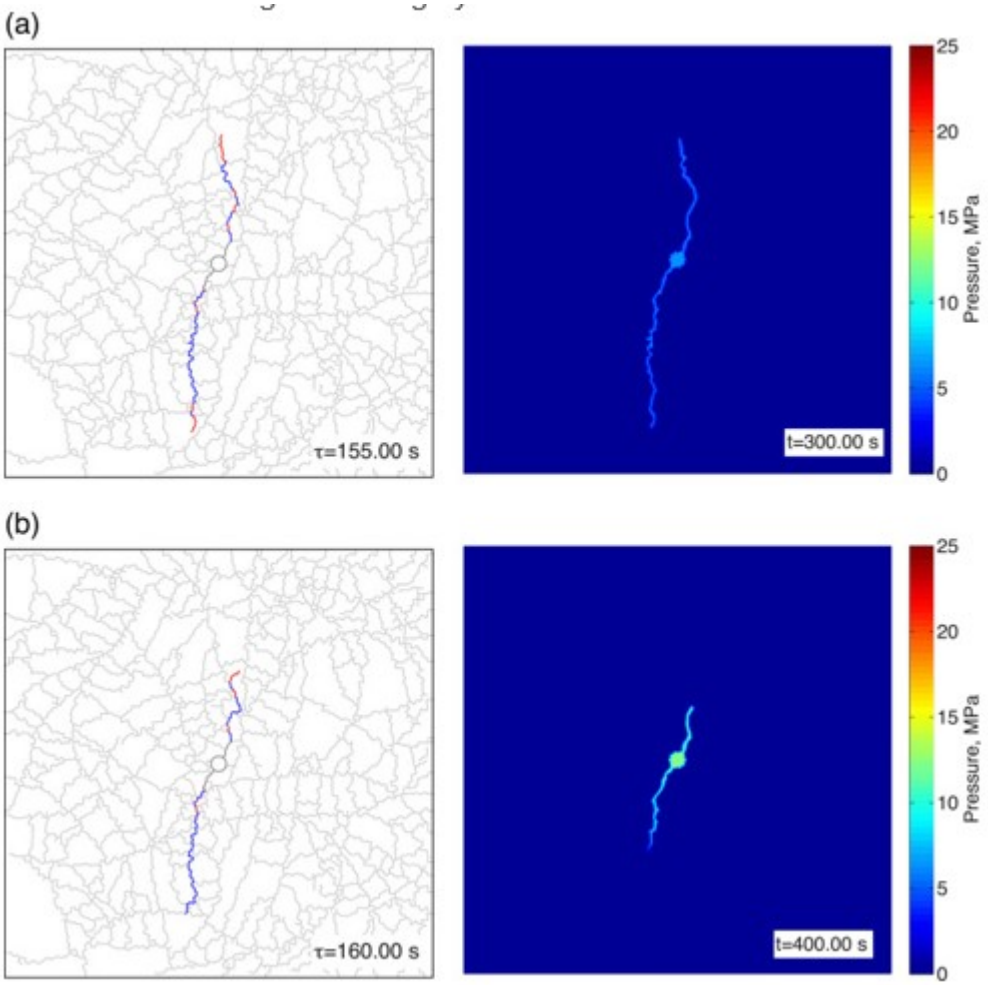

Fig. 16. Resulting fracture traces and pressure distributions at the final stage of hydraulic fracturing: a) low-viscosity water (control); and b) high-viscosity glycerol.

4.2. Strength of pre-existing fractures

The fracture strength is an important factor that can directly affects the paths of hydraulic fracture propagation in fractured media. As aforementioned in Section 3.3, the pre-existing fractures are modeled by degrading the mechanical properties of the corresponding lattice elements. Three degrees of degradation are considered here: 25% (strong), 50% (control), and 75% (weak) degradations of Young's modulus, tensile strength, and cohesive strength from the values of the intact glass material.

Fig. 17 plots the injection pressure evolution curves for the three cases of fracture strength. The initial slopes of the curves are identical for the three cases, but the fracture triggering is highly associated with the strength of pre-existing fractures. It is clearly observed that the triggering pressure increases with the strength of pre-existing fractures. However, from the curves in Fig. 17, it is rather difficult to distinguish the influence of the strength of pre-existing fractures on the fracturing characteristics. The rapid

decrease of the injection pressure may indicate a vigorous fracture growth in the case of strong fractures.

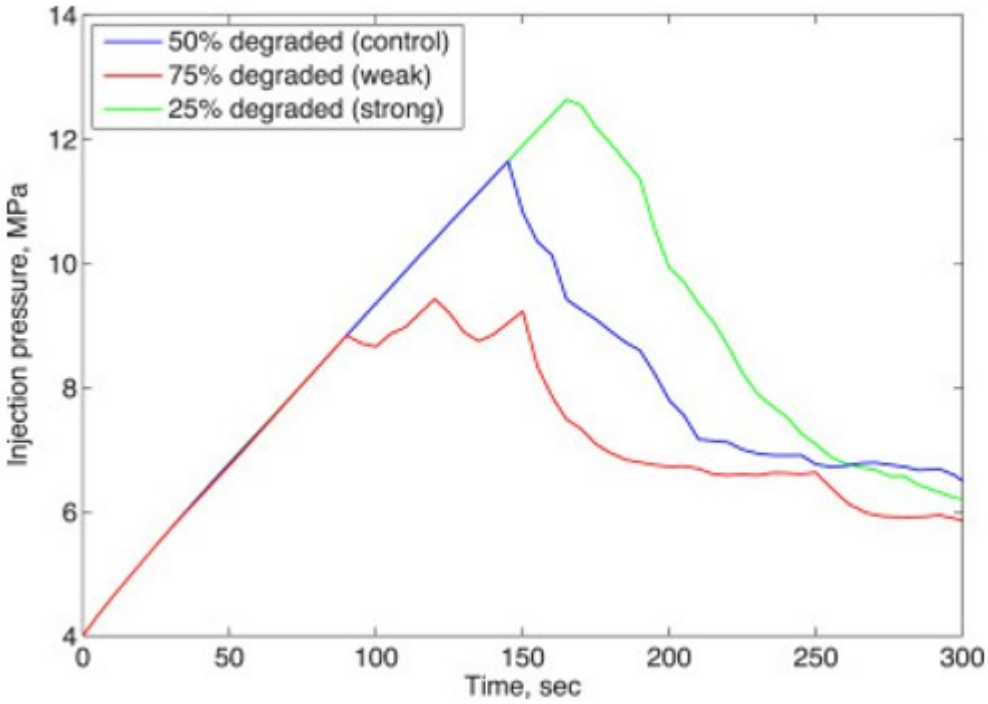

Fig. 17. Injection pressure evolutions for the cases of different degrees of strength degradation in pre-existing fractures.

Figs. 13a and 18 show a definite contrast in fracturing paths. Comparing with the fracture trace of the control, more weak fractures are activated to develop hydraulic fracture branches — more blue lines are illustrated along the main fracturing paths (Fig. 18a). Meanwhile, the fracturing paths in the case of strong fractures are controlled by the anisotropic stress condition — a considerable portion of red lines form more straight fracturing paths parallel to the maximum confining stress (Fig. 18b). Interestingly, as shown in Fig. 18a, mechanically induced cracks occur away from the main fracture branches due to stimulation of weak pre-existing fractures.

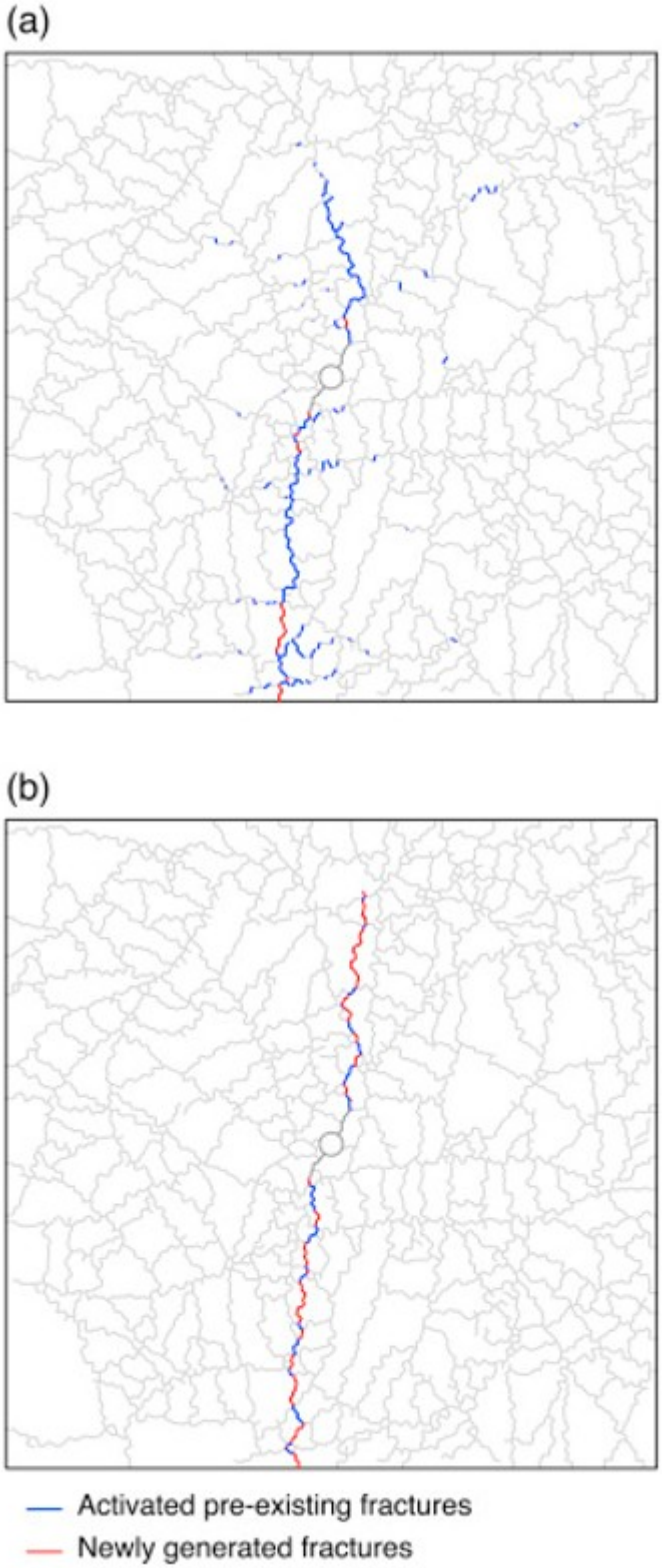

Fig. 18. Resulting fracture traces with a) weak fractures and b) strong fractures.

4.3. Confining stress conditions

In this section, the influence of the confining stress condition on hydraulic fracturing is examined with other preferential conditions (e.g., pre-existing fractures and initial notches). Three cases of confining stress conditions are considered for σx:σy=4.83:7.24MPa(control); σx=σy=4.83MPa (isotropic); and σx:σy=7.24:4.83MPa (90° rotated anisotropic).

Fig. 19 shows the injection pressure evolutions, in which the triggering pressures are compared. For the control case, the initial notches are closely aligned along the maximum confining stress, and the triggering pressure is associated with the minimum confining stress. Comparing with the triggering pressure of the control case, the isotropic stress condition does not change the triggering pressure much since the minimum confining stress is maintained at the same value. However, with a 90° rotation of anisotropic stress axes, the maximum confining stress now mainly affects the stress condition at the notch tips, therefore an increase of the triggering pressure is observed in the injection pressure evolution.

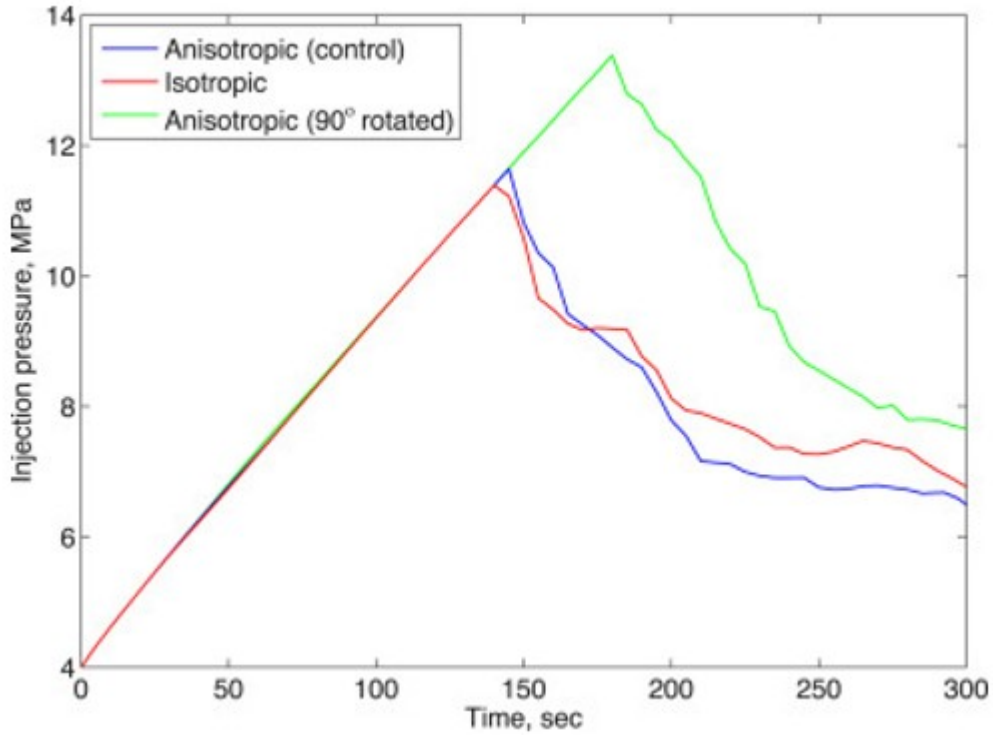

Fig. 19. Comparison of injection pressure evolutions for the cases of different confining stress conditions.

In Fig. 20, the resulting fracture traces demonstrate a distinct difference in the direction of fracturing paths. For the case of isotropic stress condition, the fracture branches advance in diagonal direction which is preferred by the notch orientation. For the case of 90° rotated anisotropic stress condition, the fracture branches initiated from the notch tips make a turn into the axis of the maximum confining stress. In both cases, fracturing occurs preferentially along pre-existing fractures, but the intact glass could be

fractured if the influence of the confining stress condition becomes dominant in the determination of local fracturing.

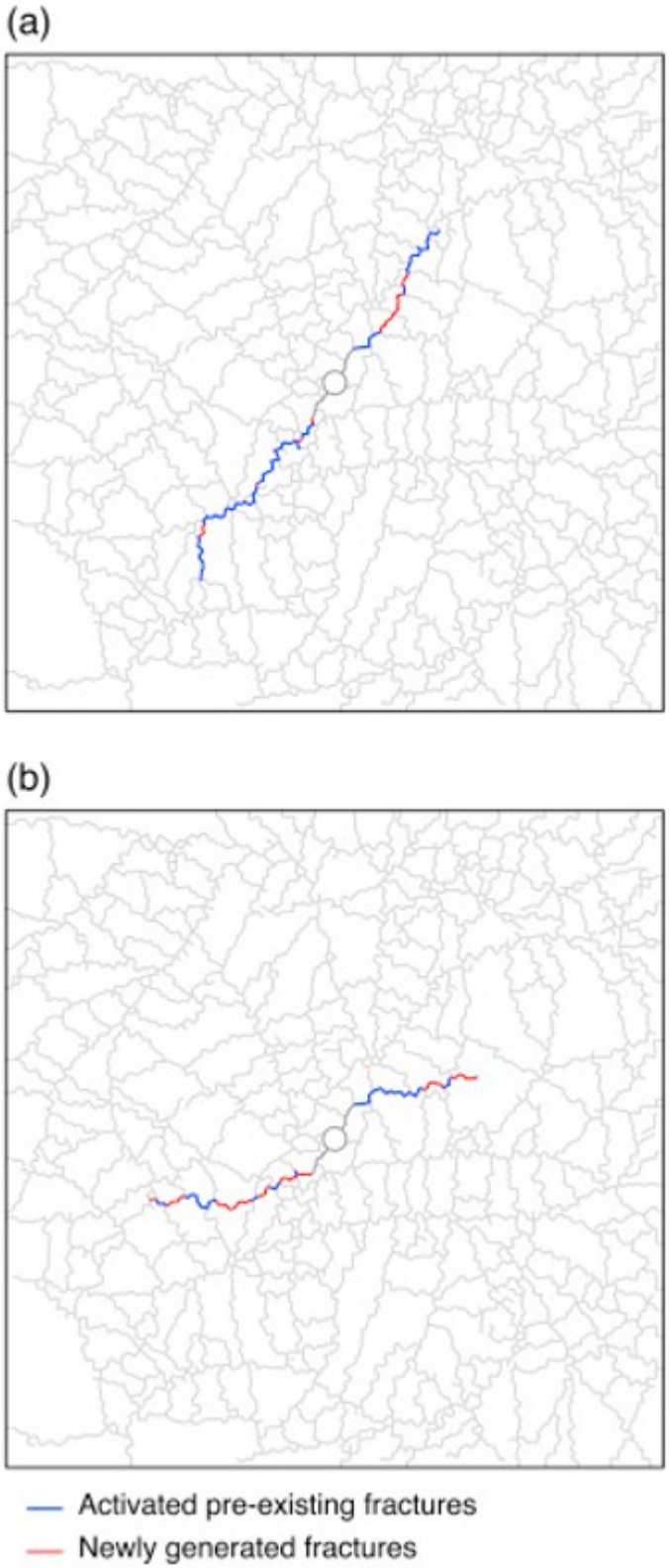

Fig. 20. Resulting fracture traces for the cases of a) isotropic stress condition (σx=σy=4.83MPa) and b) 90° rotated anisotropic stress condition (σx:σy=7.24:4.83MPa).

5. Summary and conclusions

This paper presents the implementation of an effective two-way coupling between the TOUGH2 simulator and the RBSN approach and the application to hydraulic fracturing simulations. The simulator provides a discrete representation of hydrological (fluid flow through fracture networks) and mechanical (fracture initiation and propagation) responses. The permeability of an individual fracture is rigorously evaluated from the grid geometry and the fracture aperture width. The numerical program is verified through the simulation of a fluid-driven fracture with a simple geometry, in which the fracture profiles show a good agreement with the analytical approximation based on the linear elastic fracture mechanicstheory. Subsequently, predictive and interpretative simulations are performed for hydraulic fracturing of soda-lime glass samples containing a complex pre-existing fracture network. The hydraulic fractures reproduced in the simulations compare favorably to the experimental results with respect to the injection pressure evolutions and the resulting fracture paths. Several observations and conclusions can be made:

• Pre-cracks or initial notches introduced at the injection well stabilize the hydraulic fracture propagation by decreasing the triggering pressure. This scheme can be adopted in laboratory experiments to prevent an abrupt fracture growth and control the rate of fracture propagation for better observations of fracture responses.

• Injection of high-viscosity fluid (glycerol) can also help reduce the speed of hydraulic fracture propagation, which involves a different fracturing mechanism compared to injection of low-viscosity fluid (water). For the case of high-viscosity fluid, a gap exists between the fracture tip and the fracturing fluid front, therefore the non-local effect of remote pressure is a dominant mechanism of hydraulic fracture propagation.

• The strength of pre-existing fractures impacts the details of hydraulic fracturing paths in fractured media. Main hydraulic fracturing mostly follows and activates pre-existing fractures with low strengths, whereas the hydraulic fracturing paths within high-strength fractures are more affected by confining stress conditions.

• It is generally known that the preferred direction of hydraulic fracturing is determined by the confining stress condition — perpendicular to the minimum compressive principal stress. The simulation results show a distinction of fracture directions in different confining stress conditions, which conforms to the established knowledge.

In summary, this study contributes to the further development of efficient tools for understanding the variety of characteristics in hydraulic fracture propagation. The series of simulations presented in this paper demonstrate

the modeling capabilities of the TOUGH–RBSN simulator for tightly coupled HM processes in the application of hydraulic fracture propagation. Qualitative interpretations are provided in the sensitivity analyses for the parameters that impact the features of hydraulic fracturing. For the ongoing development, a refinement could be made into the TOUGH–RBSN code to rigorously evaluate the change of fracture porosity as a response of the mechanical fracture aperture change, which will be addressed in a future study.

Acknowledgements

This research is supported by the Assistant Secretary for Fossil Energy, Office of Natural Gas and Petroleum Technology, through the National Energy Technology Laboratory, and by the Used Fuel Disposition Campaign, Office of Nuclear Energy, of the U.S. Department of Energy under Contract No. DE-AC02-05CH11231 with Lawrence Berkeley National Laboratory.

References

Adachi et al., 2007

J. Adachi, E. Siebrits, A. Peirce, J. Desroches**Computer simulation of hydraulic fractures**

Int. J. Rock Mech. Min. Sci., 44 (2007), pp. 739-757

Asahina and Bolander, 2011

D. Asahina, J.E. Bolander**Voronoi-based discretizations for fracture analysis of particulate materials**

Powder Technol., 213 (2011), pp. 92-99

Asahina et al., 2014

D. Asahina, J.E. Houseworth, J.T. Birkholzer, J. Rutqvist, J.E. Bolander**Hydro-mechanical model for wetting/drying and fracture development in geomaterials**

Comput. Geosci., 65 (2014), pp. 13-23

Asahina et al., 2011

D. Asahina, E.N. Landis, J.E. Bolander**Modeling of phase interfaces during pre-critical crack growth in concrete**

Cem. Concr. Compos., 33 (9) (2011), pp. 966-977

Bear, 1972

J. Bear**Dynamics of Fluids in Porous Media**

American Elsevier Publishing Company, New York (1972)

Biot and Willis, 1957

M.A. Biot, D.G. Willis**The elastic coefficients of the theory of consolidation**

J. Appl. Mech., 24 (1957), pp. 594-601

Bolander and Saito, 1998

J.E. Bolander, S. Saito**Fracture analyses using spring networks with random geometry**

Eng. Fract. Mech., 61 (5–6) (1998), pp. 569-591

Bossart et al., 2004

P. Bossart, T. Trick, P.M. Meier, J.-C. Mayor**Structural and hydrogeological characterisation of the excavation-disturbed zone in the Opalinus Clay (Mont Terri Project, Switzerland)**

Appl. Clay Sci., 26 (2004), pp. 429-448

Chiaramonte et al., 2008

L. Chiaramonte, M.D. Zoback, J. Friedmann, V. Stamp**Seal integrity and feasibility of CO_2 sequestration in the Teapot Dome EOR pilot: geomechanical site characterization**

Environ. Geol., 54 (8) (2008), pp. 1667-1675

Detournay, 2004

E. Detournay**Propagation regimes of fluid-driven fractures in impermeable rocks**

Int. J. Geomech., 4 (1) (2004), pp. 35-45

Freeman et al., 2011

C.M. Freeman, G.J. Moridis, T.A. Blasingame**A numerical study of microscale flow behavior in tight gas and shale gas reservoir systems**

Transp. Porous Media, 90 (1) (2011), pp. 253-268

Fu et al., 2013

P. Fu, S.M. Johnson, C.R. Carrigan**An explicitly coupled hydro-geomechanical model for simulating hydraulic fracturing in arbitrary discrete fracture networks**

Int. J. Numer. Anal. Methods Geomech., 37 (2013), pp. 2278-2300

Geertsma and de Klerk, 1969

J. Geertsma, F. de Klerk**A rapid method of predicting width and extent of hydraulically induced fractures**

J. Pet. Technol., 21 (1969), pp. 1571-1581

Kawai, 1978

T. Kawai**New discrete models and their application to seismic response analysis of structures**

Nucl. Eng. Des., 48 (1978), pp. 207-229

Khristianovic and Zheltov, 1955

Khristianovic, S.A., Zheltov, Y.P., 1955. Formation of vertical fractures by means of highly viscous fluids. In: Proceedings of 4th World Petroleum Congress, Rome., 2, pp. 579–586.

Kim and Lim, 2011

K. Kim, Y.M. Lim**Simulation of rate dependent fracture in concrete using an irregular lattice model**

Cem. Concr. Compos., 33 (9) (2011), pp. 949-955

Levasseur et al., 2010

S. Levasseur, R. Charlier, B. Frieg, F. Collin**Hydro-mechanical modelling of the excavation damaged zone around an underground excavation at Mont Terri Rock Laboratory**

Int. J. Rock Mech. Min. Sci., 47 (3) (2010), pp. 414-425

Nordgren, 1972

R.P. Nordgren**Propagation of a vertical hydraulic fracture**

Soc. Pet. Eng. J., 12 (1972), pp. 306-314

Okabe et al., 2000

Okabe, A., Boots, B., Sugihara, K., Chiu, S. N., 2000. Spatial Tessellations: Concepts and Applications of Voronoi Diagrams. John Wiley & Sons, Ltd.

Pan et al., 2014

P.-Z. Pan, J. Rutqvist, X.-T. Feng, F. Yan**TOUGH-RDCA modeling of multiple fracture interactions in caprock during CO_2 injection into a deep brine aquifer**

Comput. Geosci., 65 (2014), pp. 24-36

Perkins and Kern, 1961

T.K. Perkins, L.R. Kern**Widths of hydraulic fractures**

J. Pet. Technol., 13 (1961), pp. 937-949

Pruess et al., 2012

Pruess, K., Oldenburg, C.M., Moridis, G.J., 2012. TOUGH2 User’s Guide, Version 2. LBNL-43134 (revised).Lawrence Berkeley National Laboratory.

Rice, 1968

J.R. Rice**A path independent integral and the approximate analysis of strain concentration by notches and cracks**

J. Appl. Mech., 35 (2) (1968), pp. 379-386

Rutqvist, 2011

J. Rutqvist**Status of the TOUGH-FLAC simulator and recent applications related to coupled fluid flow and crustal deformations**

Comput. Geosci., 37 (6) (2011), pp. 739-750

Rutqvist et al., 2013

J. Rutqvist, C. Leung, A. Hoch, Y. Wang, Z. Wang**Linked multicontinuum and crack tensor approach for modeling of coupled geomechanics, fluid flow and transport in fractured rock**

J. Rock Mech. Geotech. Eng., 5 (2013), pp. 18-31

Rutqvist et al., 1998

J. Rutqvist, J. Noorishad, C.-F. Tsang, O. Stephansson**Determination of fracture storativity in hard rocks using high-pressure injection testing**

Water Resour. Res., 34 (10) (1998), pp. 2551-2560

Rutqvist and Tsang, 2002

J. Rutqvist, C.-F. Tsang**A study of caprock hydromechanical changes associated with CO_2-injection into a brine formation**

Environ. Geol., 42 (2002), pp. 296-305

Rutqvist et al., 2000

J. Rutqvist, C.-F. Tsang, O. Stephansson**Uncertainty in the maximum principal stress estimated from hydraulic fracturing measurements due to the presence of the induced fracture**

Int. J. Rock Mech. Min. Sci., 37 (2000), pp. 107-120

Rutqvist et al., 2002

J. Rutqvist, Y.-S. Wu, C.-F. Tsang, G. Bodvarsson**A modeling approach for analysis of coupled multiphase fluid flow, heat transfer, and deformation in fractured porous rock**

Int. J. Rock Mech. Min. Sci., 39 (2002), pp. 429-442

Siebrits and Peirce, 2002

E. Siebrits, A.P. Peirce**An efficient multi-layer planar 3D fracture growth algorithm using a fixed mesh approach**

Int. J. Numer. Methods Eng., 53 (2002), pp. 691-717

Wereszczak et al., 2011

Wereszczak, A.A., Fox, E.E., Morrissey, T.G., Vuono, D.J., 2011. Low velocity sphere impact of a soda lime silicate glass. Tech. Rep. ORNL/TM-2011/259, Oak Ridge National Laboratory (ORNL).

Witherspoon et al., 1980

P.A. Witherspoon, J.S.Y. Wang, K. Iwai, J.E. Gale**Validity of cubic law for fluid flow in a deformable rock fracture**

Water Resour. Res., 16 (1980), pp. 1016-1024

Yip et al., 2005

M. Yip, J. Mohle, J.E. Bolander**Automated modeling of three-dimensional structural components using irregular lattices**

Comput.-Aided Civil Infrastruct. Eng., 20 (6) (2005), pp. 393-407

Zhang et al., 2004

K. Zhang, Y.-S. Wu, G.S. Bodvarsson, H.-H. Liu**Flow focusing in unsaturated fracture networks: a numerical investigation**

Vadose Zone J., 3 (2004), pp. 624-633

Zimmermann and Reinicke, 2010

G. Zimmermann, A. Reinicke**Hydraulic stimulation of a deep sandstone reservoir to develop an Enhanced Geothermal System: laboratory and field experiments**

Geothermics, 39 (1) (2010), pp. 70-77